Aerodynamic Decelerator Systems Technology Conferences
May 16-19, 2022, Toulouse, FRANCE
26th AIAA Aerodynamic Decelerator Systems Technology Conference

10.2514/6.2022-2752

Check for updates

A fluid-structure interaction methodology to design ram-air parachutes and paragliders

Tom Lolies*
Bruce Goldsmith Design R&D, 195 avenue Auguste Renoir 06520 Magagnosc
And Dpt. of Aerodynamics, Energetics and Propulsion (DAEP), ISAE-Supaero, University of Toulouse, 10, avenue Edouard Belin - 31400 Toulouse Cedex 4 France

Miguel Charlotte†
Université de Toulouse, Institut Clément ADER, CNRS UMR 5312 INSA/UPS/ISAE-SupAero/Mines Albi, 10 Avenue Edouard Belin - BP 54032 - 31 055 TOULOUSE Cedex 4, France.

Nicolas Gourdain.‡
Dpt. of Aerodynamics, Energetics and Propulsion (DAEP), ISAE-Supaero, University of Toulouse, 10, avenue Edouard Belin - 31400 Toulouse Cedex 4 France,

Downloaded by Tom Lolies on August 17, 2022 | http://arc.aiaa.org | DOI: 10.2514/6.2022-2752

A numerical model to simulate the fluid-structure interaction of Ram-Air wings (such as gliding parachutes or paragliders) is presented. To simulate the high Reynolds number flow around the canopy a panel method is chosen. It is further enhanced using an integral boundary layer solver and a separation model to account for viscous effects. The structural model developed is a mass spring system using Delingette's identification of local stiffness parameters. The time marching of the equations of motion is carried out with a stiff integrator. A smooth shape is provided to the aerodynamic solver thanks to a surface spline of the structure. Results on a paraglider geometry are presented and compared to flight test observations. Then, a ram-air parachute canopy is studied, simulation results are challenged against wind tunnel tests.

I. Nomenclature

$\mathbf{U}_{inf}$	=	inlet velocity
Cl	=	Lift coefficient
Cd	=	Drag coefficient
Re	=	Reynolds number
S_{ref}	=	Reference area
C_p	=	Pressure coefficient
θ	=	Momentum thickness
s	=	Curvilinear chordwise coordinate
H	=	Shape parameter
H^*	=	Kinetic energy shape parameter
H^{**}	=	Density shape parameter
U_e	=	Boundary-layer edge velocity norm
M_e	=	Boundary-layer edge mach number
Re_θ	=	Momentum thickness Reynolds number
C_f	=	Dkin-friction coefficient
C_D	=	Dissipation coefficent
C_τ	=	Shear stress coefficient
δ^*	=	Displacement thickness

*Design engineer, BGD Research and Development, tom@flybgd.com
†Associate professor, ISAE-Supaero DMSM, miguel.charlotte@isae.fr
‡Associate professor, ISAE-Supaero DAEP, nicolas.gourdain@isae.fr

Copyright © 2022 by the American Institute of Aeronautics and Astronautics, Inc. All rights reserved.

S	=	Stratford's number
Re_s	=	Curvilinear coordinate reynolds number
Cp_{sep}	=	Pressure coefficient on the separation point
E, ν	=	Young's modulus and Poisson ratio
λ,μ	=	Lamé coefficients
κ,γ	=	Local stiffness parameters
β	=	Damping coefficient
dl,L,l	=	Elongation, rest length and elongated length of a Triangle's edge
σ_1, σ_2	=	Principal stresses in the fabric membrane
$\mathbf{Q}$, $\mathbf{v}$	=	Structural nodes positions and velocities
β	=	Structural damping coefficient
$\tilde{\varepsilon}$	=	Cartesian strain
$\tilde{\sigma}$	=	Cartesian stress
C_m	=	Stress-strain matrix

Downloaded by Tom Lolies on August 17, 2022 | http://arc.aiaa.org | DOI: 10.2514/6.2022-2752

II. Introduction

In order to build a thorough design tool for flexible ram-air canopies, fluid-structure interaction (FSI) can not be ignored. Indeed, since there are no major rigid parts in the structure, its shape is determined by aerodynamic pressure forces, that are themselves dependant on the shape of the structure. A major issue raised by FSI simulations for ram-air wings like paragliders and parachutes consists in properly resolving external flows with high Reynolds numbers on a flexible wall with an arbitrary motion. It is a great challenge since one needs to properly resolve a very thin turbulent boundary layer that requires very high mesh resolution close to the moving wall. N. Fogell et al. presented a framework using high-fidelity 3D CFD (Computational Fluid Dynamics) coupled to a CSD (Computational Structural Dynamics) [1], where a semi-rigid wing section is investigated. Other studies rely on ALE (Arbitrary Lagrangian Eulerian) simulations to compute the flow field around the moving boundary of the entire canopy: for instance Zhu et al. [2], proposed an approached successfully challenged against flight test data. However, in this approach, 3D resolution of the flow-field has to be computed, which is an expansive approach. ALE has also been used in other studies with for instance Zhang et al. [3], or Perin et al. [4], to simulate ram-air parachutes. Other approaches involving 3D meshes have also been suggested such as Space–Time Isogeometric Analysis by Takizawa et al. [5]. A way to work around having a 3D mesh of the fluid domain is to take advantage of low order aerodynamic models, such as potential flow codes. Previous research conducted by Chatzikonstantinou [6], Altmann [7] showed promising results. However, potential flow models do not account for viscous effects such as flow separation, that is likely to happen around parachute canopies, especially when the trailing edge is deflected as shown by Ghoreyshi et al. [8]. Such deflection is crucial when tailoring the design of ram-air wings, as the pilot controls is trajectory using steerable lines that are directly connected to the trailing edge. The steering lines are also called brake lines. Fortunately, potential flow methods can be enhanced using viscous interactions and/or flow separation models. Ortega et al. [9] obtained good results using a 3D panel method equipped with Stratford's separation model, the current work aims at developing Ortega's idea further, using a finer structural resolution (Ortega uses the same mesh for the structural and fluid equations), and also improving the 3D unsteady panel method with a boundary layer solver. This study aims at developing and validating a complete methodology to tailor the design of ram-air wings, for steady and unsteady configurations. However, only steady-states will be detailed here and further study will explore the unsteady capabilities of the code. The first section presents the computational framework, starting with the potential aerodynamic model and how it is coupled to an integral boundary layer solver and a Stratford separation criterion. The mass-spring system approach developed is then discussed. In the second second section, simulation results are presented. First, a structural mesh convergence study is presented. Second, the capability of the code to predict creases on a paraglider geometry is demonstrated. Finally, simulations of a ram-air parachute are presented and compared to wind tunnel tests.

III. Computational methodology

A. Viscous enhancement of potential flow based aerodynamics

The method developed here is a low order doublet-source unsteady panel method. Implementation of the influences, the time-stepping algorithm and of the Kutta condition as been carried-out following Katz & Plotkin (see [10], section

13.13). In the present study, the approach is further improved with an integral boundary layer (IBL) model, as proposed by Drela [11]. The following equations are solved:

$$\begin{cases} \frac{d\theta}{ds} + (2 + H - Me^2)\frac{\theta}{U_e}\frac{dU_e}{ds} = \frac{C_f}{2} \\ \theta\frac{dH^*}{ds} + [2H^{**} + H^*(1 - H)]\frac{\theta}{U_e}\frac{dU_e}{ds} = 2C_D + H^*\frac{C_f}{2} \end{cases} \tag{1}$$

With closing relations :

$$H^* = H^*(H, M_e, Re_\theta),\ H^{**} = H^{**}(H, M_e),\ C_f = C_f(H, L_e, Re_\theta),\ C_D = C_D(H, M_e, Re_\theta) \tag{2}$$

And with an additional equation, assuming the boundary layer is turbulent:

$$\frac{\delta}{C_\tau}\frac{dC_\tau}{ds} = 4.2(C_\tau eq^{1/2} - C_\tau^{1/2}) \tag{3}$$

Then, the sources are corrected using a transpiration term:

$$\sigma = \mathbf{n}.\mathbf{U}_{\text{inf}} - \frac{dU_e\delta^*}{ds} \tag{4}$$

where U_e is the external velocity and s the curvilinear coordinate. $\mathbf{n}$ is the surface normal.

To take advantage of the simplicity of these equations, the boundary layer is considered 2D on every streamline. The internal flow is not simulated. Instead, an internal pressure force is applied, assuming that the internal pressure in the canopy is given by the average of the pressure on the ram-air openings of the glider. The applicability of the fluid flow solver on arched wings such as parachutes or paragliders is challenged using the validation test case presented by Belloc [12], results are presented on fig. 2. One can notice that, for relatively low lift coefficients there is simply a small drag offset between the simulation results and the experiment. This could be explained by the fact that no wind tunnel wall corrections are computed in the original study. Furthermore, the model is not capable of simulating stall correctly, which is a standard drawback of potential flow methods. An implementation of Stratford's separation model [13] is also implemented to tackle this issue to a certain extent. Ortega's et al. [14] strategy has been employed here. Stratford's number S is computed with :

$$S(s) = \frac{2C_p(s\frac{dC_p}{ds})^{1/2}}{(10^{-6}Re_s)^{1/10}} \tag{5}$$

Finally, as proposed by Cebeci et al. [15] separation occurs if:

$$S(s) \geq 0.5 \tag{6}$$

Beyond the separation point, a simple model is applied as a post-processing step to adjust the pressure coefficients:

$$Cp(s) = Cp_{sep},\ s > s_{sep} \tag{7}$$

with s_{sep} the separation coordinate and $Cp_{sep} = Cp(s_{sep})$ the pressure coefficient at the separation point.

Finally, an empirical formula for the drag of a cylinder $Cd = f(Re)$ is used to account for the suspension lines.

B. Mass-Spring systems

For largely deformable thin flexible non-linear structures, mass-spring systems (MSS) proved to be a suitable alternative to finite element methods. Originaly introduced in the computer graphics community [16, 17] they are easy to implement, cost-efficient and fitting for high performance computing. mass-spring systems have been increasingly used to simulate thin flexible membranes [18–20], and also applied to parachute FSI [21–23].

Downloaded by Tom Lolies on August 17, 2022 | http://arc.aiaa.org | DOI: 10.2514/6.2022-2752

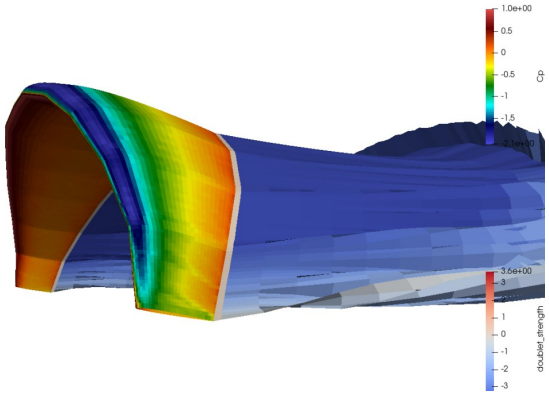


Fig. 1 Pressure coefficients obtained on the wind tunnel geometry.

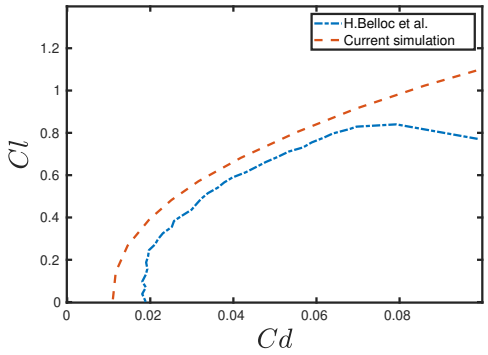


Fig. 2 Comparison between present results and H. Belloc [12] wind tunnel tests.

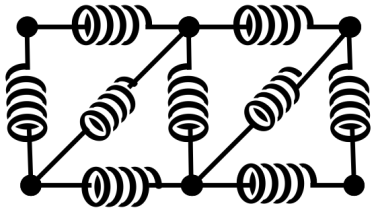


Fig. 3 Schematic description of the discrete mass-spring model.

Downloaded by Tom Lolies on August 17, 2022 | http://arc.aiaa.org | DOI: 10.2514/6.2022-2752

1. Physical model

MSS approach consists in describing the surface with a network of nodes connected by springs that reproduce the tensile behavior of the simulated material. The global mass is distributed across the nodes of the mesh. In the present study, to simplify the determination of modeling parameters, we assume that the mechanical properties of the cloth are equivalent in the chain, thread and biais directions: it is considered isotropic. Morever, the cloth is considered to be a thin membrane of constant thickness e, with standard material properties described by the Young modulus E and Poisson ratio ν. The bending stiffness is neglected in the present study.

2. Local stiffness parameters

One key issue is to determine analytically the in-plane membrane parameters, more precisely, the local spring stiffness coefficients. This involves computing deformations and forces within the triangular cells. Such an approach has been suggested by Val Gelder [24] and was later on enhanced by Delingette [25], giving an explicit expression of local stiffness parameters in a triangulated mesh for non linear membranes. This model is chosen because it directly derives from the elastic membrane model in continuum mechanics. It has also been used for parachute modeling by Shi et al. [22]. Delingette's results read for the nodal force on a node i within a triangle T_p:

$$\mathbf{F}_i(T_p) = \sum_{j\neq i} \kappa_j^{T_p} dl_j \frac{\mathbf{Q}_k - \mathbf{Q}_i}{l_j} + \sum_{j\neq i} (\gamma_k^{T_p} dl_i + \gamma_i^{T_p} dl_k) \frac{\mathbf{Q}_k - \mathbf{Q}_i}{l_j} \tag{8}$$

where the constant stiffness coefficient κ and γ are calculated using the geometry of the triangle T_p at rest :

$$\kappa_i^{T_p} = \frac{L_i^2 (2cot^2(\alpha_i(\lambda+\mu)+\mu)}{8A_p} \tag{9}$$

$$\gamma_k^{T_p} = \frac{L_i L_j (2cot\alpha_i cot\alpha_j(\lambda+\mu)-\mu)}{8A_p} \tag{10}$$

with, for a node i, $\mathbf{Q}_i$ is the deformed position vector, L_i and dl_i are the rest lengths and elongation of the opposed edge respectively, α_i is the angle within the triangle at rest shape. Then A_p is the area of T_p, and λ and μ are the lamé coefficients. Finally the internal force vector $\mathbf{F}_{int}(t, \mathbf{Q}_i, \mathbf{v}_i)$ on the node i with velocity $\mathbf{v}_i$ is calculated from the sum of the contributions from every triangles, and an added damping term:

$$\mathbf{F}_{int}(t, \mathbf{Q}_i, \mathbf{v}_i) = \sum_{T_p \in S_p} \mathbf{F}_i(T_p) + \beta \mathbf{v}_i \tag{11}$$

with β a negative damping coefficient.

The implementation of Delingette's method is validated on a square 0.2x0.2m piece of cloth, in a tensile test. Fig. 4 and 5 show how the error in Young's modulus and Poisson ratio evolves for different material configurations. One can notice that the E error is not convergent but stays near zero. The Poisson ratio error is null for $\nu = 0.33$.

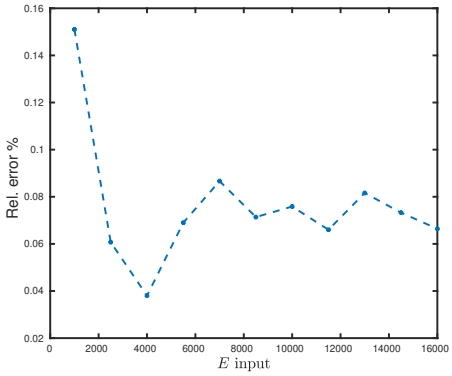


Fig. 4 Relative error measured for Young's modulus E (in Pa.m) in a tensile test, with ν = 0.3

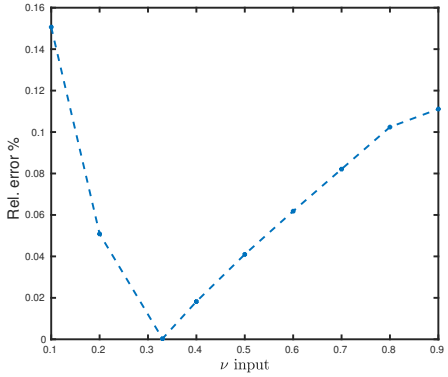


Fig. 5 Relative error measured for Poisson ratio ν in a tensile test, with E = 5000 Pa.m

3. Stress calculation

An extra post-processing step can be added to compute principal stresses, that are crucial for structural analysis and crease determination. Considering a triangle composed of the three points $(\mathbf{Q}_0, \mathbf{Q}_1, \mathbf{Q}_2)$: The natural strain vector can be defined as follows $\varepsilon_N = \begin{bmatrix} dl_1 & dl_2 & dl_3 \end{bmatrix}^T$. Also, a local basis can be defined with : $\mathbf{u} = \frac{\mathbf{Q}_1 - \mathbf{Q}_0}{||\mathbf{Q}_1 - \mathbf{Q}_0||}$ and $\tilde{\mathbf{v}} = \frac{\mathbf{Q}_2 - \mathbf{Q}_0}{||\mathbf{Q}_2 - \mathbf{Q}_0||}$. It can then be orthogonalized with a Gramm-Schmidt process: $\mathbf{v} = \tilde{\mathbf{v}} - (\tilde{\mathbf{v}}, \mathbf{u})\mathbf{u}$. Using the transformation matrix $P = \begin{bmatrix} \mathbf{u} & \mathbf{v} & \mathbf{u} \wedge \mathbf{v} \end{bmatrix}$ the 3 points of the triangle in the local coordinates can be calculated with: $\tilde{\mathbf{Q}}_i = P^T \mathbf{Q}_i$.

The conversion matrix between natural and cartesian stresses reads:

$$T = \begin{bmatrix} c_1^2 & s_1^2 & \sqrt{2} c_1 s_1 \\ c_2^2 & s_2^2 & \sqrt{2} c_2 s_2 \\ c_3^2 & s_3^2 & \sqrt{2} c_3 s_3 \end{bmatrix} \tag{12}$$

Where c_i and s_i are defined by:

$$c_i = \frac{(\tilde{\mathbf{Q}}_j - \tilde{\mathbf{Q}}_k, \mathbf{u})}{L_i}$$

$$s_i = \frac{(\tilde{\mathbf{Q}}_j - \tilde{\mathbf{Q}}_k, \mathbf{v})}{L_i}$$

The cartesian deformations can then be calculated :

$$\tilde{\varepsilon} = T^{-1} \varepsilon_N \tag{13}$$

Downloaded by Tom Lolies on August 17, 2022 | http://arc.aiaa.org | DOI: 10.2514/6.2022-2752

Finally the cartesian stresses are given by:

$$\tilde{\sigma} = \begin{bmatrix} \sigma_{xx} & \sigma_{yy} & \sigma_{xy} \end{bmatrix}^T = C_m \tilde{\varepsilon} \tag{14}$$

C_m is the stress-strain matrix:

$$C_m = \begin{bmatrix} \frac{E}{1-\nu^2} & \nu\frac{E}{1-\nu^2} & 0 \\ \nu\frac{E}{1-\nu^2} & \frac{E}{1-\nu^2} & 0 \\ 0 & 0 & \frac{E}{2(1+\nu)} \end{bmatrix} \tag{15}$$

Finally, from the Cartesian stresses, after diagonalization of 2x2 cartesian stress matrix, the principal stresses σ_1 and $\sigma_2 \leq \sigma_1$ can be obtained.

4. Crease criterion

Being non-linear by construction, the MSS approach is capable of directly resolving a buckled geometry. However, in this framework the length scales of creases can quite easily be one order of magnitude smaller than the length scale of the structural mesh. Observations from flight tests show that buckling patterns can be as small as 2mm, whereas, to keep simulation costs low, our mesh resolution does not exceed 300 to 500 points per profile perimeter which means approximately $\approx 20mm$ for a mesh element. Therefore one can only assume that the buckling pattern will be filtered by the coarse mesh resolution. A way to tackle this issue is to implement a crease model such as Pauletti's [26]. It can be applied to determine whether or not the cloth is taut or wrinkled. The crease criterion reads:

$$Criterion: \begin{cases} \text{Taut}, & \text{if } \sigma_2 > 0 \\ \text{Wrinkled}, & \text{if } \sigma_1 > 0 \geq \sigma_2 \\ \text{Slack}, & \text{if } \sigma_1 \leq 0 \end{cases} \tag{16}$$

5. Discretization

A dedicated meshing program has been implemented to triangulate ram-air geometries including internal straps, panels, lines, miniribs of paragliders and parachutes, as fig. 6 shows. The lines are modeled as individual springs. The webbing line attachments details are modeled as 3 springs, as shown in fig 7.

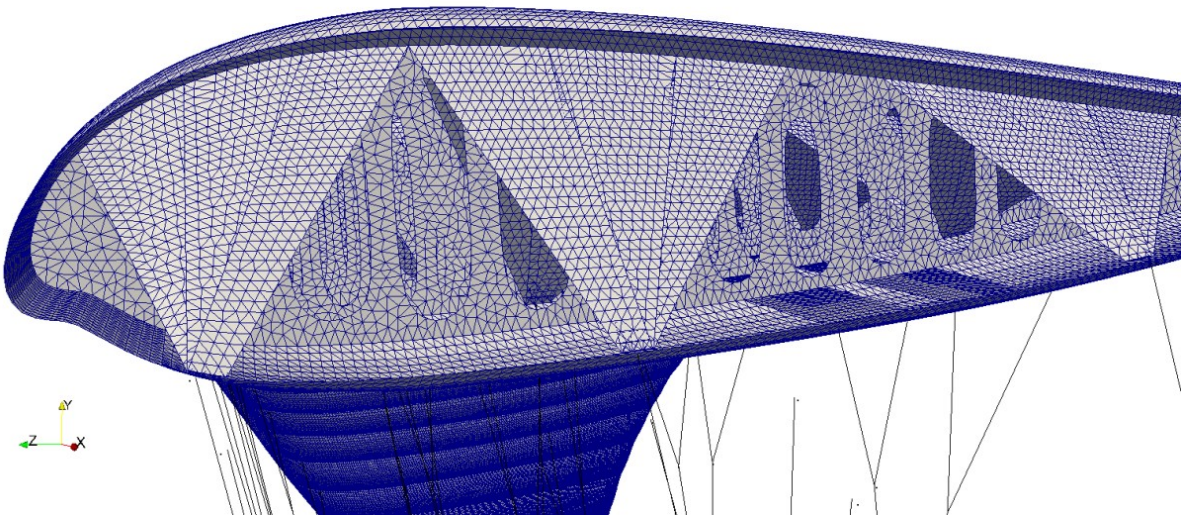


Fig. 6 Structural mesh for a paraglider geometry.

Downloaded by Tom Lolies on August 17, 2022 | http://arc.aiaa.org | DOI: 10.2514/6.2022-2752

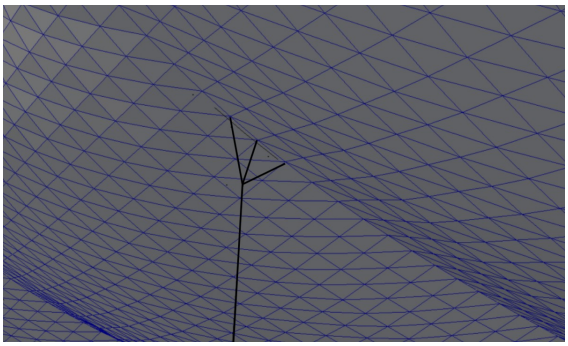


Fig. 7 Connection between a suspension line and a surface mesh. Each black line represents a spring.

6. Numerical integration

The motion of each particle is then governed by Newton's second law. Considering a particule of mass m_i with position vector $\mathbf{Q}_i$ and velocity $\mathbf{v}_i$, the equation reads:

$$m_i \frac{d^2\mathbf{Q}_i(t)}{dt^2} = \mathbf{F}_{int}(t, \mathbf{Q}_i, \mathbf{v}_i) + \mathbf{F}_{ext}(t, \mathbf{Q}_i, \mathbf{v}_i) \tag{17}$$

where $\mathbf{F}_{int}(t, \mathbf{Q}_i, \mathbf{v}_i)$ and $\mathbf{F}_{ext}(t, \mathbf{Q}_i, \mathbf{v}_i)$ are the internal and external force vectors acting on the particle. Then, compiling eq. 17 for all nodes in the MSS, we get:

$$M \frac{d^2\mathbf{Q}(t)}{dt^2} = \mathbf{F}_{int}(t, \mathbf{Q}, \mathbf{v}) + \mathbf{F}_{ext}(t, \mathbf{Q}, \mathbf{v}) \tag{18}$$

here, $\mathbf{Q}$ and $\mathbf{v}$ contain the coordinates and velocities for every point in the mesh respectively. M is a diagonal mass matrix. One advantage of MSS shown here is that they do not require mass-lumping, as M is inherently diagonal.

Time integration of the eq. 18 is a key aspect of the simulation. Indeed, the stiffness of the cloth is high and the mass is low. Therefore the inner time scales of the structure oscillations will be very short as their order of magnitude is given by:

$$T_0 \approx 2\pi\sqrt{\frac{m}{k}} \tag{19}$$

Therefore keeping a stable simulation without reducing the time step extensively is a challenging task, as the system is very stiff to integrate. Numerical integration of stiff systems has been studied by Hairer et al. [27]. A solution presented is to use stiff numerical integrators such as implicit Runge-Kutta methods. They have a high order of accuracy with great stability properties even with large timesteps. The time stepping algorithm works as follows:

$$y' = f(t, y) \tag{20}$$

$$y_1 = y_0 + h\sum_{i=1}^{s} b_i k_i \tag{21}$$

$$k_i = f(t_0 + hc_i, y_0 + \sum_{j=1}^{s} a_{ij} k_j) \tag{22}$$

where $f(t, y)$ is deduced from Eq.18, the generalization of the procedure above for second order derivatives is detailed in [28]. k_i are the substeps computed at each time step. the coefficients to compute the substeps are given in the Butcher matrix :

Downloaded by Tom Lolies on August 17, 2022 | http://arc.aiaa.org | DOI: 10.2514/6.2022-2752

$$
\begin{array}{c|cccc}
c_1 & a_{11} & a_{12} & \dots & a_{1s} \\
c_2 & a_{21} & a_{22} & \dots & a_{2s} \\
.. & & & & \\
c_s & a_{s1} & a_{s2} & \dots & a_{ss} \\
\hline
 & b_1 & b_2 & \dots & b_s
\end{array}
$$

any non-zero coefficient a_{ij} with $i \leq j$ means that Eq.22 will have to be solved implicitly using a Newton optimization loop involving the Jacobian matrix. The diagonally implicit L-Stable ESDIRK4 scheme [29] is used here. The Butcher table for this integrator reads :

$$
\begin{array}{c|ccccc}
\frac{1}{4} & \frac{1}{4} & & & & \\
\frac{3}{4} & \frac{1}{2} & \frac{1}{4} & & & \\
\frac{11}{20} & \frac{17}{50} & -\frac{1}{25} & \frac{1}{4} & & \\
\frac{1}{2} & \frac{371}{1360} & -\frac{137}{2720} & \frac{15}{544} & \frac{1}{4} & \\
1 & \frac{25}{24} & -\frac{49}{48} & \frac{125}{16} & -\frac{85}{12} & \frac{1}{4} \\
\hline
 & \frac{25}{24} & -\frac{49}{48} & \frac{125}{16} & -\frac{85}{12} & \frac{1}{4}
\end{array}
$$

C. Coupling strategies

On the one hand, some authors chose high fidelity aerodynamics methods, that, despite of their high simulation costs, can provide a very stable fluid-structure interface coupling using the immersed boundary method [30], [20], [31]. Regarding coupling with inviscid solvers Ortega et al. [9] proposed a methodology where the structural and aerodynamic meshes are the same. This simplifies the simulation as no interpolation schemes are required. In the present study, a different approach is preferred for the two following reasons:

- First, since the structural solver does not require inverting a large dense matrix the membrane surface mesh can be much finer than the aerodynamic mesh. Mesh convergence study (see section IV.A) showed that for a typical paraglider geometry the number of structural nodes required is one order of magnitude above the number of surface panels in the fluid mesh.
- Second, the 3D panel method is likely to produce inaccurate results and numerical artefacts when dealing with greatly deforming non linear bodies and rough surfaces. Hence, the smoothness of the geometry plays a major role in the accuracy and stability of the simulations.

These elements suggest that interpolations between the two sub-systems are required. The simulation results will then greatly depend on how accurately they are carried out. Indeed, a conservative formulation is key in FSI modelling, as Farhat et al. [32] showed. Here, the structural geometry, only C^0 in general, is approximated with smooth surface splines. The implementation used is proposed by the C++ tinynurbs library, based on Piegl & Tiller theory [33]. In the following section, the surface spline refers to the continuous surface approximation of the structural geometry, that is then sampled to generate the aerodynamic panels.

Differences between aerodynamic and structural meshes are outlined in figures 8-11. One can notice that the splining procedure successfully removes creases and complex deformations of the structural mesh. Nevertheless, the real shape of the structure is inevitably altered, therefore accurately preserving the force and energy balance between the two sub-systems is a challenging issue, since the geometry and the mesh resolutions are different. The coupling scheme to update structural forces works in three steps.

- First, the structural mesh is projected on the surface spline.
- Second, local surfaces dS_{proj} and normal vectors $\mathbf{n}_{proj}$ are calculated on the projected structural geometry.
- Third, 5 surface splines are generated to interpolate from the panels the pressure coefficients Cp, friction coefficients Cf and the three components of the normalized surface velocity $\mathbf{s}$ (that gives the orientation of the local friction force).
- Fourth, the 5 splines are sampled on the projected structural point, then local forces can then be calculated on every node $\mathbf{f}^i_{ext} = 0.5\rho V^2(Cp_{tot}\mathbf{n}_{proj} + Cf\mathbf{s})dS_{proj}$. Where $Cp_{tot} = Cp + Cp_{int}$ with Cp_{int} the internal pressure coefficient, assumed to be the average of the pressure coefficients on the opening area.

Indeed fig. 12 shows the differences in local lift coefficient distribution on the canopy. The total lift error in this configuration is 0.4%.

Downloaded by Tom Lolies on August 17, 2022 | http://arc.aiaa.org | DOI: 10.2514/6.2022-2752

Downloaded by Tom Lolies on August 17, 2022 | http://arc.aiaa.org | DOI: 10.2514/6.2022-2752

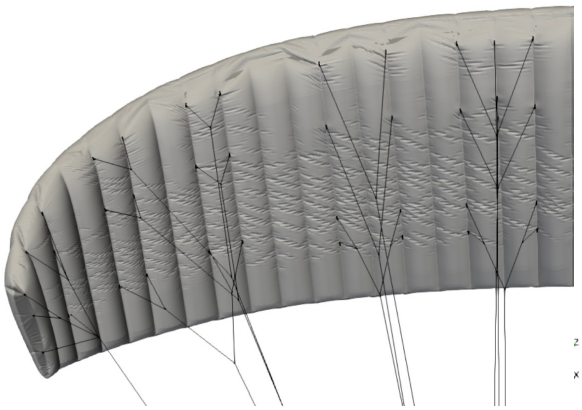


Fig. 8 Structural mesh for paraglider geometry.

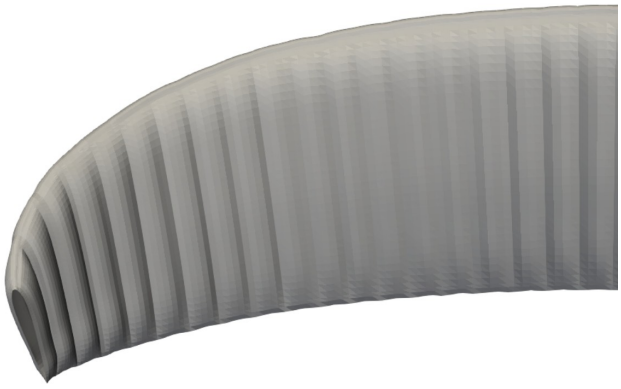


Fig. 9 Resplined paraglider aerodynamic mesh.

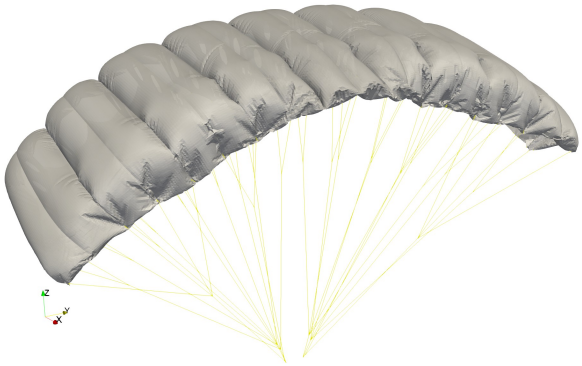


Fig. 10 Structural mesh for a parachute geometry

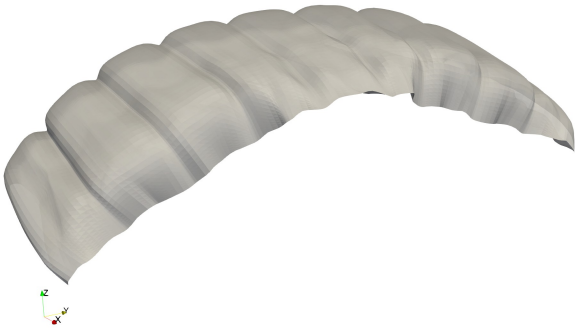


Fig. 11 Resplined parachute aerodynamic mesh

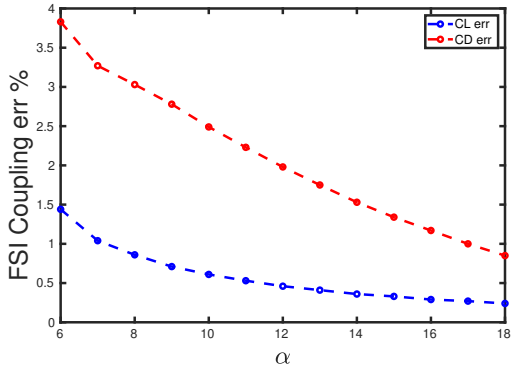


Fig. 12 Error for lift and drag coefficients in the structural and aerodynamic meshes.

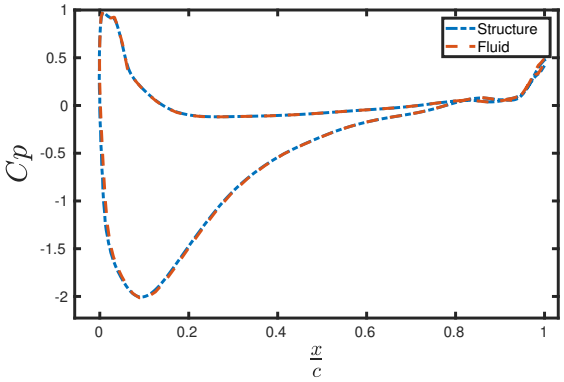


Fig. 13 Pressure coefficients on a section of the canopy from the structural and aerodynamic perspectives.

fig 12 shows how the coupling lift and drag error evolves according to angle of attack α. One can notice that the error is relatively small for higher α that are relevant to the flight envelope of paragliders. Also, fig. 13 demonstrates how small the differences between the aerodynamic and structural pressure coefficients are. However even very accurate Cp and Cf interpolations can lead to non zero drag error because of the low numerical precision of the body-force integration. This is for the same reason that some authors not interested in FSI problems and viscous effects choose to integrate body forces in the Trefftz plane instead to improve numerical accuracy [34]. More effort to reduce coupling

errors further might be necessary when dealing with fast unsteady cases, which is not the target of the present study. Since we are mostly interested in steady state converged solutions any artificial creation or destruction of energy between the fluid and structure subsystems does not affect the final solution significantly. The coupling procedure used in the following simulations is a simple first order conventional serial staggered (CSS) procedure as presented by Farhat et al. [35]. More accurate schemes will be required when the transient phase is of first importance. Moreover, since the aerodynamic timestep is typically two orders of magnitude greater than the structural timestep due to the stiff integration problem, a sub-cycling procedure is employed for the structural solver.

IV. Results and discussion.

Our current work aims at validating the simulation approach with wind tunnel experiments and flight test results.

A. Effect of mesh convergence.

A paraglider test case is considered. 3 mesh sizes are investigated, reported in the table below:

Mesh	coarse	medium	fine
Structural nodes	162127	373953	803506
Fluid nodes	25300	25300	25300
Simulation time (hours)	6	12	30

The simulations have been conducted on a desktop work station equipped with AMD Ryzen Threadripper 3960X 24-Core Processor.

In this section, only the effect of the structural resolution is considered. The triangulation of the cloth surface does not include areas that are specifically refined. Fig. 14 shows how the mesh size in the coarse configuration is too large compared to the length scale of stress gradients. Moreover, one can notice that the trace of the rib holes in the stress field is not visible in the coarse simulation. Therefore part of the results are filtered.

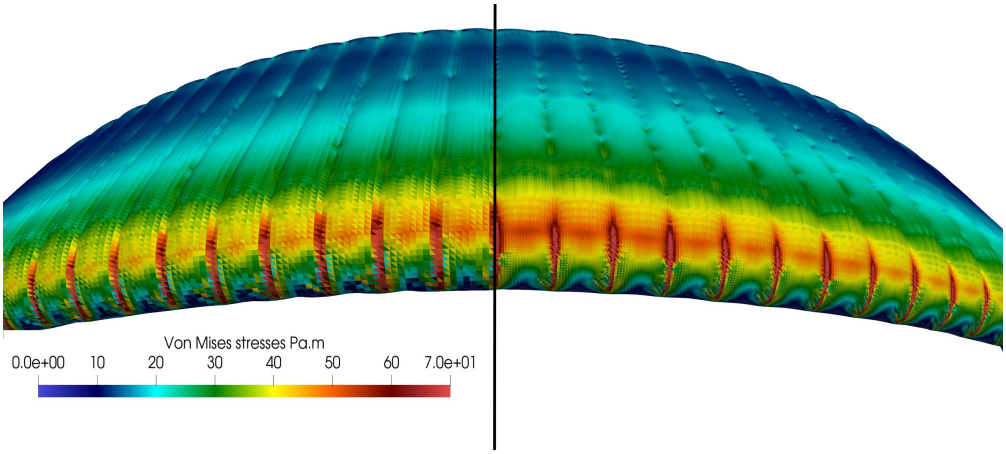


Fig. 14 Effect of mesh resolution on Von mises stresses rendering. Left = coarse, Right = fine

Moreover, fig. 15 shows how the crease criterion (areas in red correspond to $\sigma_1 > 0 \geq \sigma_2$) activates differently in the coarse or fine configurations. Since the stress field is affected by the lack of resolution in the coarse configuration, it is not surprising that the crease prediction is altered as well.

In fig. 16 the creased regions in the medium or fine configurations are very similar. Also, fig. 17 shows not only the angle of attack but also the lateral position of every rib in the paraglider geometry. One can notice in fig. 17 that whereas the coarse points are located in very different positions, the medium and fine ribs are superimposed at the same locations and with the same angle of attack. Combined with what can be seen on fig 16, where the creased areas are nearly identical between medium and fine meshes, these elements suggest that the fine configuration is converged.

Downloaded by Tom Lolies on August 17, 2022 | http://arc.aiaa.org | DOI: 10.2514/6.2022-2752

Downloaded by Tom Lolies on August 17, 2022 | http://arc.aiaa.org | DOI: 10.2514/6.2022-2752

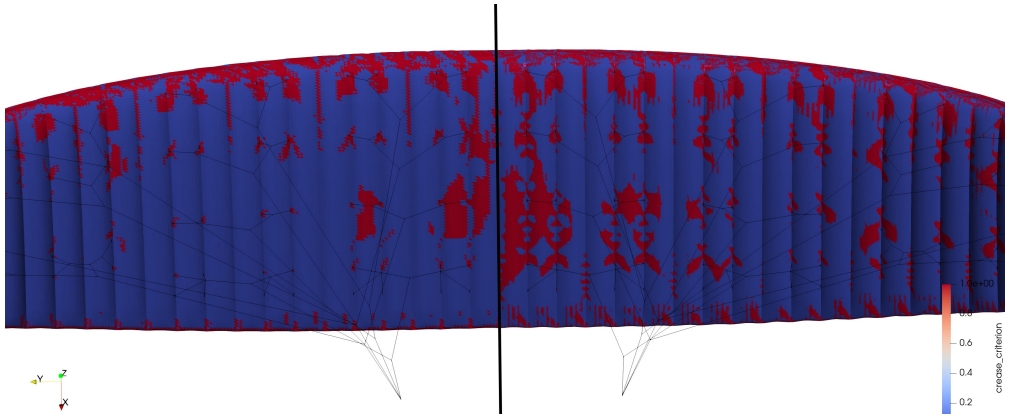


Fig. 15 Effect of mesh resolution on crease criterion activation. Left = coarse, Right = fine

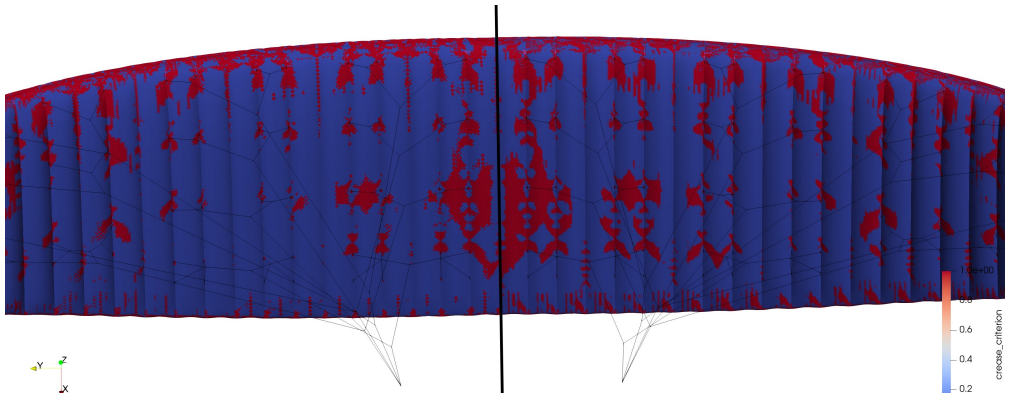


Fig. 16 Effect of mesh resolution on crease criterion activation. Left = medium, Right = fine

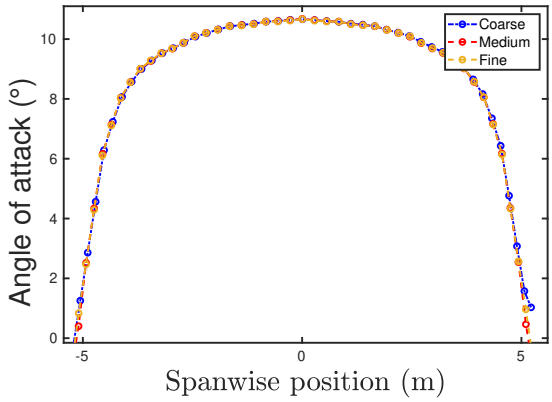


Fig. 17 Local angle of attack distribution for each rib section

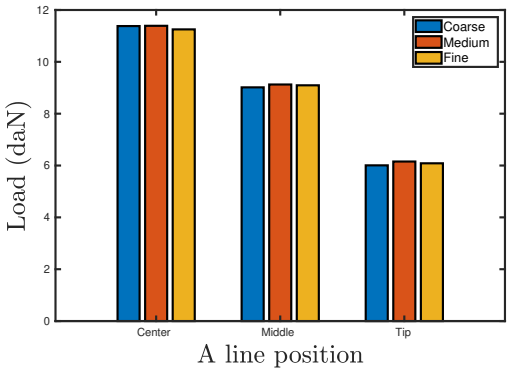


Fig. 18 Load on main A lines

Finally, the line loads are not mesh-convergent as fig. 18 shows. This result was to be expected since the lines are defined as individual springs: they are constructed the same way regardless of the cloth mesh resolution.

B. Crease prediction on paragliders.

To showcase the capabilities of the methodology, a rejected prototype shown flying in fig. 19 is analyzed here. The glider suffered from a significant crease mostly between B and C lines on the lower sail, the crease is visible from the pilot's perspective, a close up view can be found in fig. 21.

In the present simulation, the risers are fixed Dirichlet's conditions. An inlet velocity of 10.8 m/s is applied. This velocity is measured using a speed probe during the trim speed flight tests. This simple setup is drawn in fig. 20. The simulation parameters are summarized in the chart below:

Mesh	Struct. nodes	Aero. nodes	S_{ref}	Re	E	ν	U_{inf}
Paraglider	480000	15000	$25m^2$	2.10^6	100000Pa.m	0.3	10.8 m/s



Fig. 19 The rejected prototype in flight

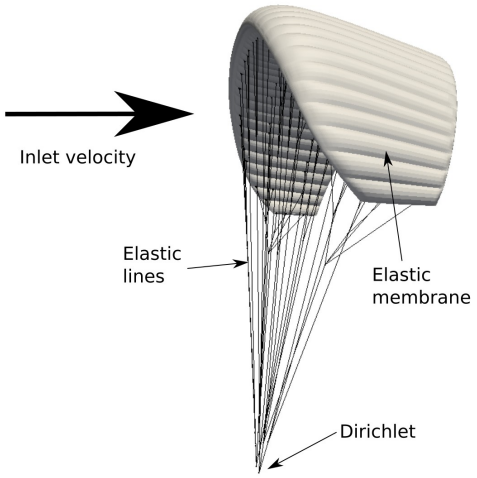


Fig. 20 Schematic representation of the simulation setup

Fig. 21 also shows the crease criterion distribution from the simulation results. Red areas correspond to wrinkled criterion in eq. 16. Here, the simulation successfully predicts a crease between B and C lines like on the prototype.

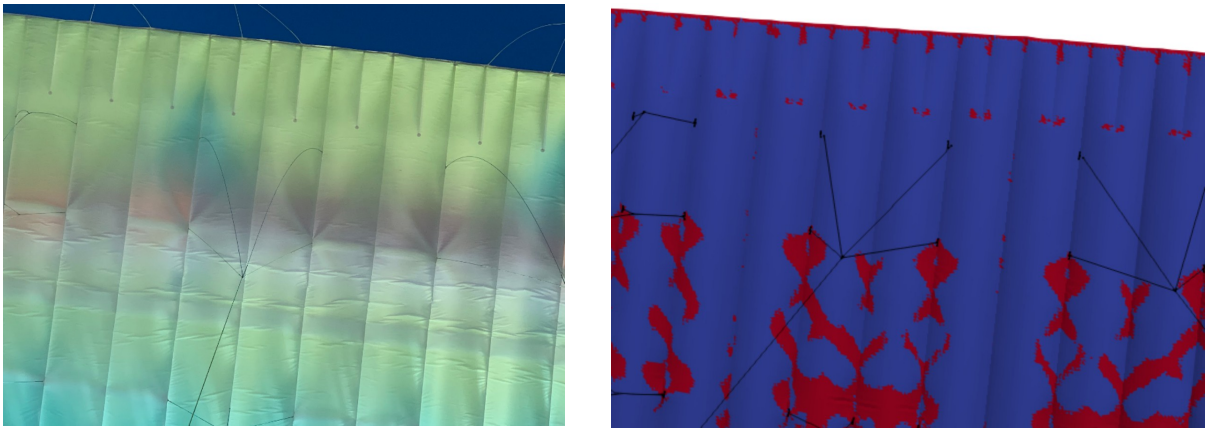


Fig. 21 Close up view of the lower surface crease (left: flight test, right: simulation)

Such predictive modeling tool can then be used to avoid unexpected crease are deformations on future prototypes.

Downloaded by Tom Lolies on August 17, 2022 | http://arc.aiaa.org | DOI: 10.2514/6.2022-2752

C. Parachute simulation

Simulation of parachutes is a very challenging topic compared to paragliders, as they undergo much larger deformations. In the present study, a parachute model, for which extensive wind tunnel test results are available, is considered.

1. Experimental setup

Experiments have been conducted in 2014 by H. Belloc and described in an unpublished internal report. A 1/3.6 scaled parachute model was tested in the S4 Eiffel type (open vein) wind tunnel in Toulouse. The reference area chosen is 3.225 m^2 and the inlet velocity is 11 m/s . A dedicated scale was designed to measure lift and drag. Drag corrections were applied to account for the wind tunnel boundary conditions. The brake deflection is defined as zero when the trailing edge is on the limit of being deflected. Several configurations for brake deflection were studied, reported in the chart below :

Scale model deflection (mm)	0	50	100	150	200
Real parachute (mm)	0	180	360	540	720
dimensionless	0%	4.5%	9%	13.5%	18%

2. Simulation results.

The simulation setup is similar to the wind tunnel case, where the risers are fixed and a constant horizontal wind is applied, which is the same as in fig. 20. As the parachute studied here does not have any billow in the design, the initial configuration of the geometry is with flat panels. The billowing phase is therefore simulated until convergence is reached, when the pitch moment converges to zero as in fig. 25. The inflation phase is described in figs. 22-24. Each simulation is conducted with 130000 points in the structure and 17000 aerodynamic panels, and runs for about 10hours on the AMD 24-Core processor.

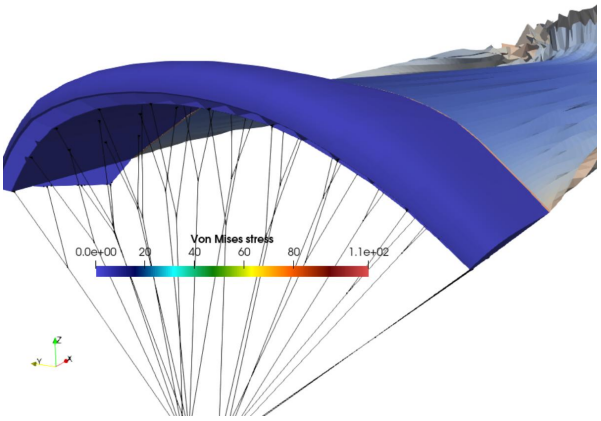


Fig. 22 Parachute simulation before the FSI iterations start.

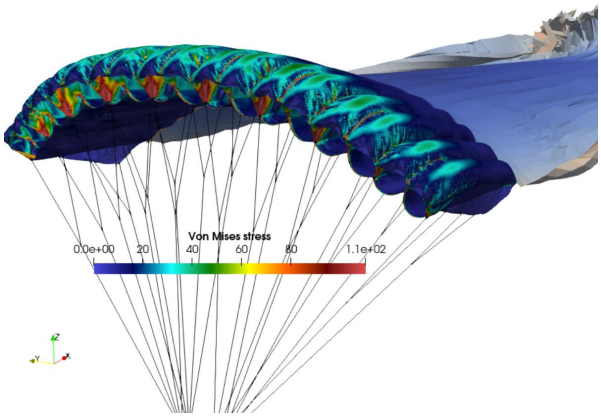


Fig. 23 The FSI simulation is starting, the geometry billows progressively.

When the geometry billows, the aerodynamic panels follow the shape of the structure and the mesh refinement is adapted accordingly, with finer mesh near the rib sections. The parachute is then simulated in 5 different brake configurations: no brakes (trailing edge not deflected), 4.5% brakes, 9% brakes, 13.5% brakes and finally 18%. Including brakes in the simulation involves a near 90 degree deflection of the wing's trailing edge in the chord-wise direction which is a very difficult configuration to simulate, especially when using potential flow-based methods.

The wind tunnel tests do not contain any shape measurement devices, this is why the shape validation is mostly based on qualitative comparisons from pictures taken during the tests. In fig. 26, the leading edge view shows how the opening shape is well captured by the simulation: one can notice that slack tip panels found experimentally have a similar shape in the simulation, and that the taut panels of the center are also well captured by the simulation. Trailing

Downloaded by Tom Lolies on August 17, 2022 | http://arc.aiaa.org | DOI: 10.2514/6.2022-2752

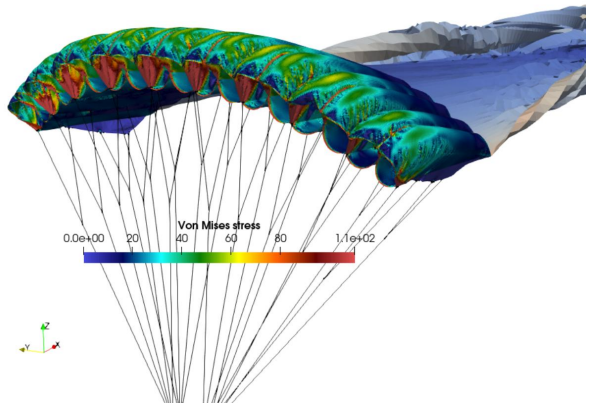


Fig. 24 Shape of the structure for 0% brake deflection colored with Von Mises stresses after convergence

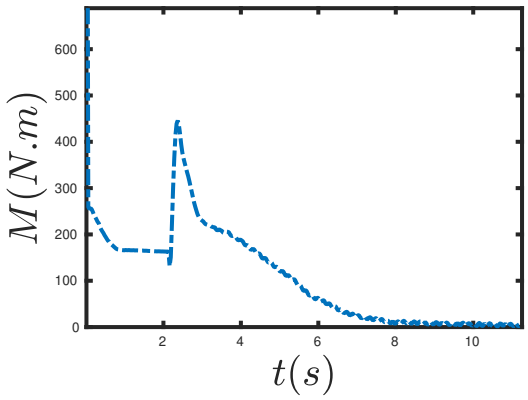


Fig. 25 Evolution of pitch moment coefficient during FSI iterations

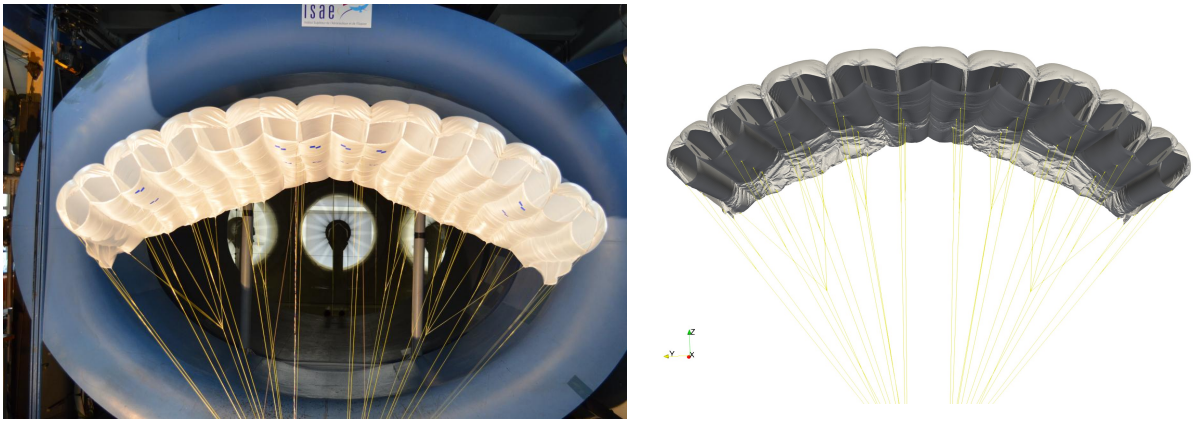


Fig. 26 Leading-edge view of the parachute with 18% brakes in the wind tunnel tests. (left: wind tunnel test, right: simulation)

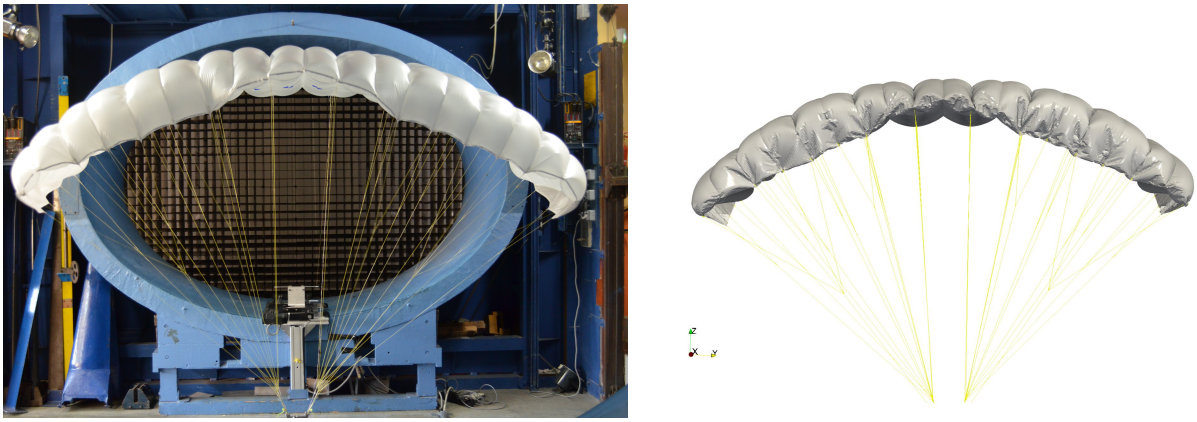


Fig. 27 Trailing-edge view of the parachute with 18% brakes in the wind tunnel tests (left: wind tunnel test, right: simulation)

edge views of fig. 27-28 show the details of the deflected area when brakes are applied. In the simulation, the stabilizers are not inflated properly because no aerodynamic pressure forces are applied on these parts.

For each configuration, once the pitch moment is converged the lift and drag coefficients are exported and compared

Downloaded by Tom Lolies on August 17, 2022 | http://arc.aiaa.org | DOI: 10.2514/6.2022-2752

Downloaded by Tom Lolies on August 17, 2022 | http://arc.aiaa.org | DOI: 10.2514/6.2022-2752

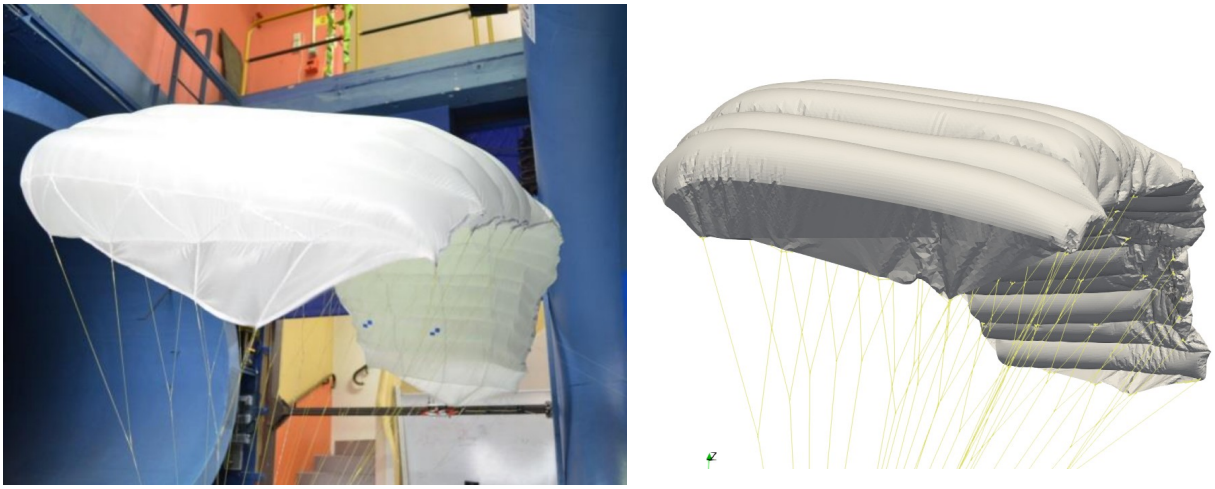


Fig. 28 The parachute with 13.5% brakes in the wind tunnel tests (left: wind tunnel test, right: simulation)

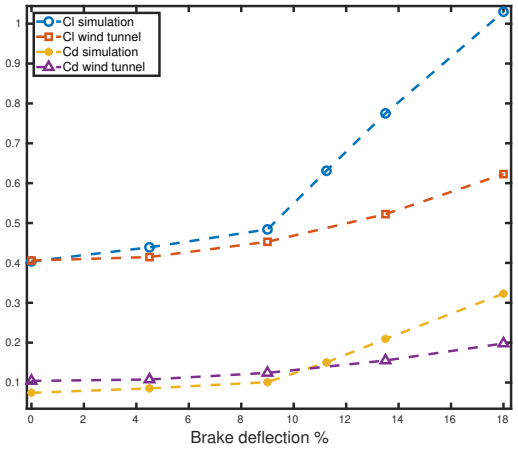


Fig. 29 Effect of brake deflection on aerodynamic coefficients without any separation model

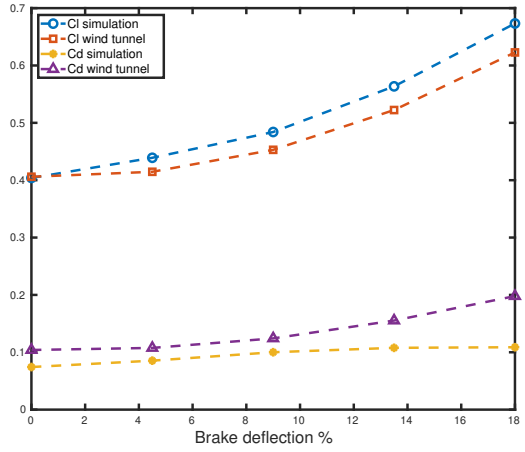


Fig. 30 Effect of brake deflection on aerodynamic ceofficients using Stratford's model.

to the results found in the wind tunnel tests. Fig. 29 shows how the panel method with viscous interactions compare to the wind tunnel results. One can notice that the lift is well captured with zero or low trailing edge deflections. Indeed, there is a Cl error of 0.5% without brakes that then reaches 6% with a 9% brake deflection. However, there is more error regarding drag coefficient. The error stays close to 20% in that same low-deflection range. This error can be caused by several issues in the modeling assumptions. First, there is no leading edge separation bubble, and in general any effect the opening might have on the external flow is neglected. Although this assumption is not critical for paragliders, as Belloc et al. suggested [36] it might lead to greater errors for parachute configurations. Second, the drag induced by the opening vents (because of the internal pressure) is not very precisely simulated since the internal pressure is just assumed to be constant and equal to the external pressure found above the opening vent area. Finally, to maintain a stable simulation, the trailing edge is sharpened in the aerodynamic mesh (see fig. 11) which could be a cause for under-estimating pressure drag induced by flow separation in the vicinity of the highly billowed trailing edge of this parachute. The lift and drag error increases tremendously as the brake deflection goes beyond 10% in fig 29. This is easily explained by the fact that the boundary layer equations break down on the top surface when the deflection starts near the trailing edge: there is flow separation, and the integral boundary layer resolution fails. The potential flow then artificially follows a near 90 degree deflection and thus generates an exaggerated amount of lift in the trailing edge region. This is why the activation of the separation model given by eq. 6 is critical, as shown in fig. 30: the *Cl*

error stays reasonable even with 18% brake deflection where it reaches a maximum of 8%. However the separation model shows a tendency to under-estimate drag: the drag does not increase as much as it should and the Cd error rises from 20% with 9% brake deflection to 40% in the 18% brake deflection case. A possible suggestion to explain this issue is that the empirical pressure correction of eq. 7 successfully predict a higher pressure drag, however, the induced drag is also possibly affected in an inaccurate way since the separation model is only a post processing step and there is no feedback loop between the separation phenomenon and the potential flow based induced drag calculation. This parachute study shows that using potential flow based aerodynamic solver to tackle the design issues of parachute is a very interesting approach since it is capable of providing interesting insights on glider's deformations, wrinkles and aerodynamic coefficients with very reasonable simulations costs.

V. Conclusion and future work

A fast simulation design tool has been developed, that relies on a 3D unsteady panel method coupled with an integral boundary layer flow solver to simulate the external flow. Aerodynamic effects of trailing edge deflection can be accounted for thanks to a Stratford separation model, that adjusts the pressure coefficients when the boundary layer equations brake down. The structural model is a mass-spring system. Local stiffness parameters are determined using Delingette's theory. The FSI coupling method is a conventional staggered serial procedure that can only be expected to be first-order in time, but the present study is for now only focused on converged steady states. Results on a paraglider geometry show that the method is mesh convergent and can be used as a predictive tool to anticipate undesired deformations or wrinkles on a paraglider geometry. This model is currently being employed extensively in a paraglider design office. Moreover, the method can also be applied on parachutes even though the core assumptions behind the code are less adapted to canopies that have a larger opening, a thick blunt trailing edge and undergo larger deformations. However the results are very promising showing realistic deformations and accurate prediction of the lift coefficient for different brake deflections, even if there is a significant error for drag coefficient prediction. Further work is then required to improve the present study. For paragliders, line load and shape measurements will be conducted to challenge the simulation results further. Regarding parachute simulations, more precise shape validation needs to be performed to confirm the accuracy of the structural results. Finally, the shape obtained after convergence with FSI in the present study will be simulated in a 3D aerodynamics-only solver (using RANS or LES models) that will be more suited to simulate high lift aerodynamics. Future work will indeed investigate the use of a combination of low-order FSI and high fidelity aerodynamics solvers to provide a reliable, cost-efficient design office simulation framework.

Downloaded by Tom Lolies on August 17, 2022 | http://arc.aiaa.org | DOI: 10.2514/6.2022-2752

Acknowledgments

The authors would like to thank Hervé Belloc for the experimental data and the academic support, Basile Périn from the DGA (Direction Générale de l'Armement) for approving the co-funding of this research, and Arna and Bruce Goldsmith and Christoph Scheer from BGD for the extensive support, trust, equipment, and funding.

References

[1] Fogell, N. A., Iannucci, L., and Bergeron, K., "Fluid-Structure Interaction Simulation study of a Semi-Rigid Ram-Air Parachute Model," American Institute of Aeronautics and Astronautics (AIAA), 2017. https://doi.org/10.2514/6.2017-3547.

[2] Zhu, H., Sun, Q., Tao, J., Chen, Z., Dehmer, M., and Xie, G., "Flexible modeling of parafoil delivery system in wind environments," *Communications in Nonlinear Science and Numerical Simulation*, Vol. 108, 2022, p. 106210. https://doi.org/10.1016/j.cnsns.2021.106210, URL https://doi.org/10.1016/j.cnsns.2021.106210.

[3] Zhang, S. Y., Yu, L., Wu, Z. H., Jia, H., and Liu, X., "Numerical investigation of ram-air parachutes inflation with fluid-structure interaction method in wind environments," *Aerospace Science and Technology*, Vol. 109, 2021. https://doi.org/10.1016/j.ast.2020.106400.

[4] Perin, B., Belloc, H., Bordenave, P., Larrieu, C., and Simond, C., "Fluid-Structure Interaction Simulation of Ram Air Parachutes - An Application for a Kite -," American Institute of Aeronautics and Astronautics (AIAA), 2015. https://doi.org/10.2514/6.2015-2185.

[5] Takizawa, K., Tezduyar, T. E., and Terahara, T., "Ram-air parachute structural and fluid mechanics computations with the Space–Time Isogeometric Analysis (ST-IGA)," *Computers and Fluids*, Vol. 141, 2016, pp. 191–200. https://doi.org/10.1016/j.compfluid.2016.05.027.

[6] Chatzikonstantinou, T., "Recent Advances in the Numerical Analysis of Ram Air Wings - The Three Dimensional Simulation code PARA3D", American Institute of Aeronautics and Astronautics (AIAA)," *AIAA-93-1203*, 1993.

[7] Altmann, H., "Fluid-Structure Interaction Analysis of Ram-Air Parafoil Wings," American Institute of Aeronautics and Astronautics (AIAA), 2015. https://doi.org/10.2514/6.2015-2184.

[8] Ghoreyshi, M., Bergeron, K., Jirasek, A., Seidel, J., Lofthouse, A. J., and Cummings, R. M., "Computational aerodynamic modeling for flight dynamics simulation of ram-air parachutes," *Aerospace Science and Technology*, Vol. 54, 2016, pp. 286–301. https://doi.org/10.1016/j.ast.2016.04.024, URL http://dx.doi.org/10.1016/j.ast.2016.04.024.

[9] Ortega, E., Flores, R., and Pons-Prats, J., "Ram-Air Parachute Simulation with Panel Methods and Staggered Coupling," *Journal of Aircraft*, Vol. 54, No. 2, 2016, pp. 807–814. https://doi.org/10.2514/1.c033677.

[10] Katz, J., and Plotkin, A., "Low-Speed Aerodynamics," *Flight Physics*, 2001. https://doi.org/10.1007/978-1-4020-8664-9_3.

[11] Drela, M., and Giles, M. B., "Viscous-inviscid analysis of transonic and low Reynolds number airfoils," *AIAA Journal*, Vol. 25, No. 10, 1987, pp. 1347–1355. https://doi.org/10.2514/3.9789.

[12] Belloc, H., "Wind tunnel investigation of a rigid paraglider reference wing," *Journal of Aircraft*, Vol. 52, No. 2, 2015, pp. 703–708. https://doi.org/10.2514/1.C032513.

[13] Stratford, B. S., "Flow in the Laminar Boundary Layer near Separation," *Aeronautical Research Council Reports and Memoranda*, , No. 3002, 1954.

[14] Ortega, E., Flores, R., Cuartero, E., and Oñate, E., "Efficient aeroelastic analysis of inflatable structures using enhanced potential flow aerodynamics," *Journal of Fluids and Structures*, Vol. 90, 2019, pp. 230–245. https://doi.org/10.1016/j.jfluidstructs.2019.06.013, URL https://doi.org/10.1016/j.jfluidstructs.2019.06.013.

[15] Cebeci, T., Mosinskis, G. J., and Smith, A. M., "Calculation of separation points in incompressible turbulent flows," *Journal of Aircraft*, Vol. 9, No. 9, 1972, pp. 618–624. https://doi.org/10.2514/3.59049.

[16] Provot, X., "Deformation constraints in a mass-spring model to describe rigid cloth behavior," *Proceedings - Graphics Interface*, 1995, pp. 147–154. URL http://www-rocq.inria.fr/syntim/research/provot/.

[17] Nealen, A., Müller, M., Keiser, R., Boxerman, E., and Carlson, M., "Physically based deformable models in computer graphics," *Computer Graphics Forum*, Vol. 25, No. 4, 2006, pp. 809–836. https://doi.org/10.1111/j.1467-8659.2006.01000.x.

[18] Okuizumi, N., "Numerical simulations of centrifugal deployments of membranes by spring-mass system models," *Collection of Technical Papers - AIAA/ASME/ASCE/AHS/ASC Structures, Structural Dynamics and Materials Conference*, American Institute of Aeronautics and Astronautics (AIAA), 2010. https://doi.org/10.2514/6.2010-2583.

[19] Chen, M., and Boyle, F. J., "Investigation of membrane mechanics using spring networks: Application to red-blood-cell modelling," *Materials Science and Engineering C*, Vol. 43, 2014, pp. 506–516. https://doi.org/10.1016/j.msec.2014.07.043.

[20] de Tullio, M. D., and Pascazio, G., "A moving-least-squares immersed boundary method for simulating the fluid–structure interaction of elastic bodies with arbitrary thickness," *Journal of Computational Physics*, Vol. 325, 2016, pp. 201–225. https://doi.org/10.1016/j.jcp.2016.08.020, URL http://dx.doi.org/10.1016/j.jcp.2016.08.020.

[21] Benney, R. J., and Stein, K. R., "Computational fluid-structure interaction model for parachute inflation," *Journal of Aircraft*, Vol. 33, No. 4, 1996, pp. 730–736. https://doi.org/10.2514/3.47008, URL http://arc.aiaa.org.

[22] Shi, Q., Reasor, D., Gao, Z., Li, X., and Charles, R., "On the verification and validation of a spring fabric for modeling parachute inflation," *Journal of Fluids and Structures 58 (2015)20–39*, 2015.

[23] Kim, J. D., Li, Y., and Li, X., "Simulation of parachute FSI using the front tracking method," *Journal of Fluids and Structures*, Vol. 37, 2013, pp. 100–119. https://doi.org/10.1016/j.jfluidstructs.2012.08.011.

[24] Van Gelder, A., "Approximate simulation of elastic membranes by triangulated spring meshes," *Journal of Graphics tools, 3(2):21-42*, 1998.

[25] Delingette, H., "Triangular springs for modeling nonlinear membranes," *IEEE Transactions on Visualization and Computer Graphics*, Vol. 14, 2008, pp. 329–341. https://doi.org/10.1109/TVCG.2007.70431.

Downloaded by Tom Lolies on August 17, 2022 | http://arc.aiaa.org | DOI: 10.2514/6.2022-2752

[26] Pauletti, R. M., and Guirardi, D. M., "Implementation of a simple wrinkling model into argyris membrane finite element," *Textile Composites and Inflatable Structures VI - Proceedings of the 6th International Conference on Textile Composites and Inflatable Structures, Structures Membranes 2013*, 2013, pp. 142–153.

[27] Hairer, E., and Wanner, G., "Runge–Kutta Methods, Explicit, Implicit," *Encyclopedia of Applied and Computational Mathematics*, Springer Berlin Heidelberg, 2015, pp. 1282–1285. https://doi.org/10.1007/978-3-540-70529-1_144.

[28] Jay, L. O., and Petzold, L. R., "Highly oscillatory systems and periodic-stability," 1998.

[29] Hairer, E., and Wanner, G., *Solving Ordinary Differential Equations II*, Springer Series in Computational Mathematics, 2000.

[30] Rabinovitch, J., Huang, D. Z., Borker, R., Avery, P., Farhat, C., Derkevorkian, A., and Peterson, L., "Towards a Validated FSI Computational Framework for Supersonic Parachute Deployments," *AIAA Aviation 2019 Forum*, American Institute of Aeronautics and Astronautics, Reston, Virginia, 2019. https://doi.org/10.2514/6.2019-3275, URL https://arc.aiaa.org/doi/10.2514/6.2019-3275.

[31] Suzuki, K., Minami, K., and Inamuro, T., "Lift and thrust generation by a butterfly-like flapping wing-body model: Immersed boundary-lattice Boltzmann simulations," *Journal of Fluid Mechanics*, Vol. 767, 2015, pp. 659–695. https://doi.org/10.1017/jfm.2015.57.

[32] Farhat, C., Lesoinne, M., and Le Tallec, P., "Computer methods in applied mechanics and engineerlng Load and motion transfer algorithms for fluid/ structure interaction problems with non-matching discrete interfaces: Momentum and energy conservation, optimal discretization and application to aeroelasticity," Tech. rep., 1998.

[33] Piegl, L., and Tiller, W., "The NURBS book," *Choice Reviews Online*, Vol. 35, No. 02, 1997, pp. 35–0952–35–0952. https://doi.org/10.5860/choice.35-0952, URL http://link.springer.com/10.1007/978-3-642-97385-7.

[34] Drela, M., and Kohler, T. J., "Power balance in aerodynamic flows," *AIAA Journal*, Vol. 47, No. 7, 2009, pp. 1761–1771. https://doi.org/10.2514/1.42409.

[35] Farhat, C., van der Zee, K. G., and Geuzaine, P., "Provably second-order time-accurate loosely-coupled solution algorithms for transient nonlinear computational aeroelasticity," *Computer Methods in Applied Mechanics and Engineering*, Vol. 195, No. 17-18, 2006, pp. 1973–2001. https://doi.org/10.1016/J.CMA.2004.11.031, URL https://www.sciencedirect.com/science/article/pii/S0045782505001945.

[36] Meyer Forsting, A., Sgarbossa, F., Manara, F., Chapin, V., and Belloc, H., "Influence of the air inlet configuration on the performances of a paraglider open airfoil," *International Journal of Aerodynamics*, Vol. 5, No. 2, 2016, p. 83. https://doi.org/10.1504/ijad.2016.10001536.

Downloaded by Tom Lolies on August 17, 2022 | http://arc.aiaa.org | DOI: 10.2514/6.2022-2752